EES Catalysis

Accepted Manuscript

This article can be cited before page numbers have been issued, to do this please use: W. Ma, X. Hu, J. Tian and Q. Xu, *EES Catal.*, 2026, DOI: 10.1039/D6EY00121A.

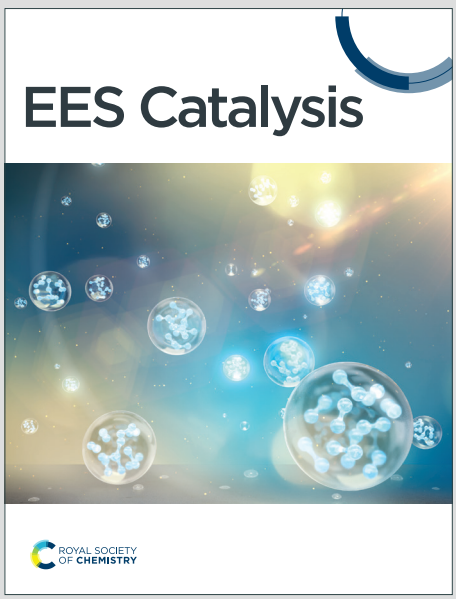

View Article Online
DOI: 10.1039/D6EY00121A

Broader context statement.

High temperature solid oxide electrochemical cells have emerged as a promising technology for CO_2 electroreduction, thanks to their 100% product selectivity and very high energy efficiency (typically 80%+). However, most of the reported progress in CO_2 electroreduction is made on lab-scale cells, typically of 1 x 1 cm^2, with a power of 1-2 W. While the transition from laboratory-scale cells to large-area demonstrators is critical to the development of this technology, this transition is extremely challenging due to scale-dependent mechanical and fabrication limitations. In this paper, we report a systematic engineering approach to address this challenge and demonstrate it on $La_{0.8}Sr_{0.2}Ga_{0.8}Mg_{0.2}O_{3-x}$ (LSGM) electrolyte-supported cells, a platform chosen due to the electrolyte's relatively low mechanical strength yet excellent ionic conductivity. By developing a multi-stage sintering protocol with carefully optimized heating ramps and dwell times, we achieve crack-free LSGM electrolytes with large areas. By homogenizing contact pressures during cell assembly, we eliminate stress concentration points. The combined effectiveness of these strategies results in a 5-cell stack operating at more than 200 W and with a high energy efficiency more than 90%.

View Article Online
DOI: 10.1039/D6EY00121A

ARTICLE

Up-Scaling of Electrolyte-Supported Solid Oxide Electrolysis Cells for CO_2 Reduction

Received 00th January 20xx,
Accepted 00th January 20xx

DOI: 10.1039/x0xx00000x

Jiaming Tian,[a] Wenchao Ma [a], Qiucheng Xu and Xile Hu [*a]

CO_2 electrolysis to CO by solid oxide electrolysis cells (SOECs) is a promising route for producing sustainable chemicals and fuels using renewable electricity. $La_{0.8}Sr_{0.2}Ga_{0.8}Mg_{0.2}O_{3-x}$ (LSGM)-based electrolyte-supported cells (ESCs) are an attractive configuration in SOEC because they enable flexible electrode choices, offering industrially relevant current density, energy efficiency, and long-term stability at high temperatures. While ESCs with a thin LGSM electrolyte layer demonstrates high efficiency at a small size (1 W), the fabrication, assembly, and testing of large cells are challenging: cracks may form due to sintering stress, and uneven pressure distribution during mounting can cause failure. Here, we address these challenges through a systematic engineering. A controlled stress-release sintering protocol prevents electrolyte cracking. A pressure distribution analysis and the subsequent addition of compressive buffer layers mitigate localized pressure and avoid structural failure. We obtain a 5 × 5 cm^2 LSGM-based ESC that achieves 1 A/cm^2 at 1.21 V and demonstrates 950-hour stability. Furthermore, we assemble a 5-cell stack that delivers a peak electrolysis power of 225 W, enabling a CO output of ~1.13 kg/day. This work establishes a scalable and mechanically reliable pathway for translating high-performance LSGM ESC concepts from single cells to stack-level operation under CO_2 electrolysis conditionsbstract text goes here.

Introduction

The electrochemical conversion of CO_2 into syngas (CO + H_2) or hydrocarbons offers a promising pathway to close the carbon cycle while storing intermittent renewable energy.[1-2] Among various electrolysis cells, high-temperature CO_2 electrolysis in solid oxide electrolysis cells (SOECs) leverages enhanced reaction kinetics (current density > 1A/cm^2) and favorable thermodynamics (energy efficiency > 80%) at 600–800 °C, making it a compelling solution for industrial-scale applications.[3-5]

In the context of CO_2 electrolysis, solid oxide electrolysis cells (SOECs) are commonly configured either as cathode-supported cells (CSCs) or electrolyte-supported cells (ESCs).[6] Another alternative configuration, the metal-supported cells (MSCs), remain at an early stage of development, and their requirement for high-temperature sintering under H_2 atmosphere presents inherent challenges for upscaling.[7-8] In CSCs, a porous Ni/yttria-stabilized zirconia (YSZ) support provides strong mechanical strength, with functional layers (electrolyte and counter electrode) deposited on top. Due to the chemical and mechanical constraints imposed by the YSZ backbone, only Ni/YSZ and Ni/gadolinium-doped ceria (GDC) catalysts are compatible in CSCs.[9] However, both catalysts suffer from insufficient activity for CO_2 electrolysis, while carbon deposition on Ni catalysts and Ni particle migration further accelerate performance degradation.[10] In contrast to CSCs, ESCs employ a dense electrolyte layer, typically 200–500 μm thick,[11-12] as the structural backbone, while catalysts are coated on both sides. This configuration decouples electrode choice from the mechanical support, allowing the integration of advanced electrode materials and improving reactivity as well as tolerance to carbon deposition.[13-15] For ESCs, YSZ is the conventional electrolyte, yet its relatively low ionic conductivity at intermediate temperatures (0.03 S/cm at 800 °C) and limited electrode compatibility impose significant performance constraints.[16] GDC offers higher O^{2-} conductivity (0.1 S/cm at 800 °C), but partial reduction of Ce^{4+} to Ce^{3+} introduces electronic leakage that lowers the overall efficiency.[16-17] $La_{0.8}Sr_{0.2}Ga_{0.8}Mg_{0.2}O_{3-x}$ (LSGM), by comparison, exhibits superior O^{2-} conductivity (0.15 S/cm at 800 °C) without electronic leakage.[18-19] Although interfacial diffusion of transition metals into LSGM can occur at elevated temperatures,[16] interposing a thin ceria-based buffer layer effectively suppresses this interdiffusion,[14] enabling stable integration of a wide range of advanced catalysts, such as Ni-Fe-$La_{0.6}Sr_{0.4}Fe_{0.8}Mn_{0.2}O_3$,[12] FeNi-$(La_{0.6}Sr_{0.4})_{0.95}Co_{0.2}Fe_{0.8}O_{3-x}$,[20] $Pr_{0.4}Sr_{0.16}(NiFe)_{1.5}Mo_{0.5}O_{3-x}$,[13]

[a] Laboratory of Inorganic Synthesis and Catalysis, Institute of Chemical Sciences and Engineering, Ecole Polytechnique Fédérale de Lausanne (EPFL), Lausanne 1015, Switzerland.
E-mail: xile.hu@epfl.ch
Supplementary Information available

View Article Online
DOI: 10.1039/D6EY00121A

$(La_{0.75}Sr_{0.25})_{0.97}Cr_{0.5}Mn_{0.5}O_3@Ce_{0.6}Mn_{0.3}Fe_{0.1}O_2$,[14] $Co_{0.5}Ni_{0.5}@Ce_{0.8}Sm_{0.2}O_{2-x}$.[3] However, the benefits of LSGM ESCs come with challenges: their poor mechanical strength and large sintering shrinkage complicate fabrication and scaling, with most demonstrations to date limited to cells below 1 cm^2. A few larger LSGM cells were reported, but they operate in the fuel-cell mode at modest current densities, which did not offer sufficient insights into the fabrication of large-area cells for electrolysis.[21]

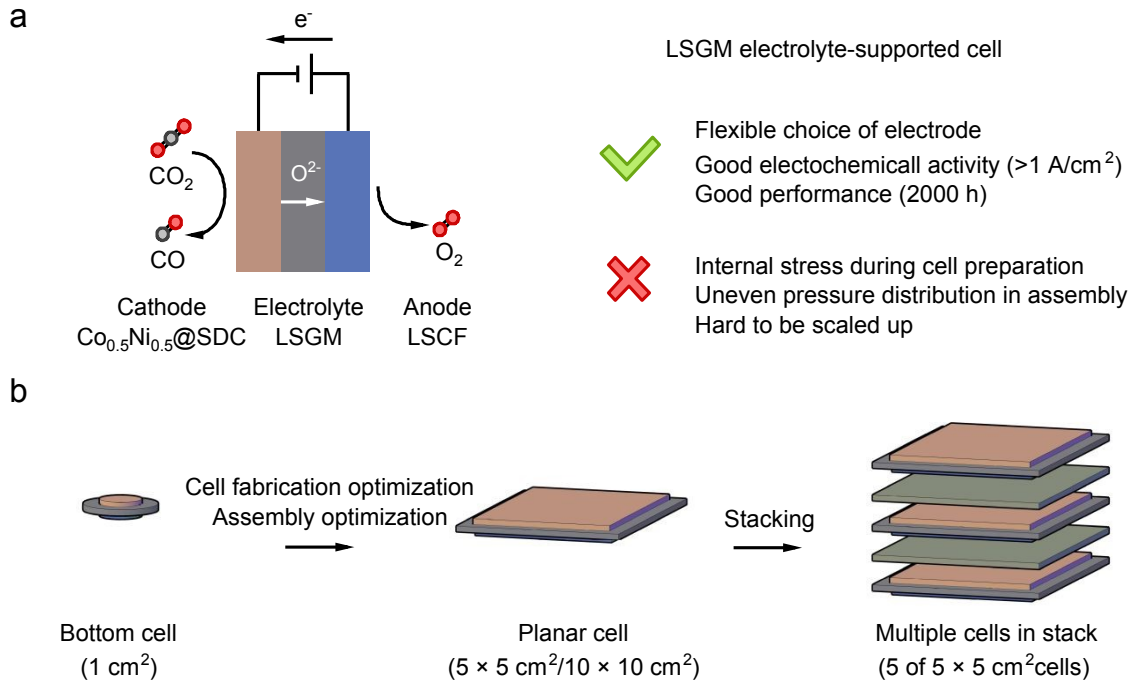

Fig. 1 Schematic of LSGM electrolyte-supported cells. (a) Configuration and key characteristics of an LSGM electrolyte-supported cell, highlighting its electrode flexibility, electrochemical performance, and associated mechanical challenges during fabrication and assembly. (b), Strategy for scaling up from a laboratory-scale button cell (1 cm^2) to a planar cell (5 × 5 cm^2 and 10 × 10 cm^2) and ultimately to a multi-cell stack (5 of 5 × 5 cm^2 cells), enabled by systematic engineering.

Despite the rapidly improving electrochemical performance of LSGM-based SOECs at the button cell level (~1 cm^2), their translation to large-area cells (>10 cm^2) and stack configurations has remained extremely limited (Fig. 1a). In practice, electrolyte-supported fabrication is particularly susceptible to warping or cracking during sintering due to un controllable thermal stress evolution,[22-23] as well as mechanical failure induced by non-uniform contact pressure during stack assembly.[24] These scale-dependent limitations have historically constrained most reported LSGM-based ESCs to research-scale dimensions around 1 cm^2.[13,14,20]

In this work, we address this gap by systematically investigating the fabrication- and assembly-related mechanical constraints that govern the scalability of LSGM electrolyte-supported SOECs for CO_2 electrolysis (Fig. 1b). Our objective is to identify, quantify, and mitigate the dominant failure modes that emerge uniquely during upscaling. By integrating stress-release sintering, pressure-distribution analysis, and mechanically compliant buffer layers, we establish a transferable engineering framework that enables reliable electrochemical evaluation of large-area LSGM ESCs and their short stacks. This approach provides essential design insights for bridging the gap between laboratory-scale demonstrations and mechanically robust stack-level operation.

Results and discussion

Upscaling of the fabrication of LSGM ESCs

The fabrication of large-area LSGM ESCs follows a multi-step process involving tape-casting, electrolyte sintering, electrode deposition, and final cell sintering (Fig. S1a).[3,23] While the tape-casting method is straightforward to scale up, achieving electrolyte

View Article Online
DOI: 10.1039/D6EY00121A

flatness and managing residual stress during sintering are universal challenges in ceramic electrolyte fabrication.[24-26] These challenges are, however, significantly amplified for LSGM due to its large sintering shrinkage (~20%) and inferior mechanical strength compared to conventional YSZ electrolytes, making crack formation and warping far more severe when scaling beyond button-cell dimensions. The sintering process involves multiple stages that generate complex internal stresses, including binder burnout during low-temperature processing, as well as shrinkage and densification at high temperatures.[24] Each of these stages contributes to stress development through distinct physical processes: organic removal creates porous weak regions,[25] while non-uniform shrinkage and anisotropic grain growth during densification introduce localized strain fields.[26] These effects become particularly pronounced in thin (<200 μm) large-area electrolytes where constrained boundary conditions prevent stress relaxation. The resulting stresses accumulate, leading to various failure modes ranging from mild warping to severe cracking or catastrophic fracture, undermining the feasibility of manufacturing upscaled cells.

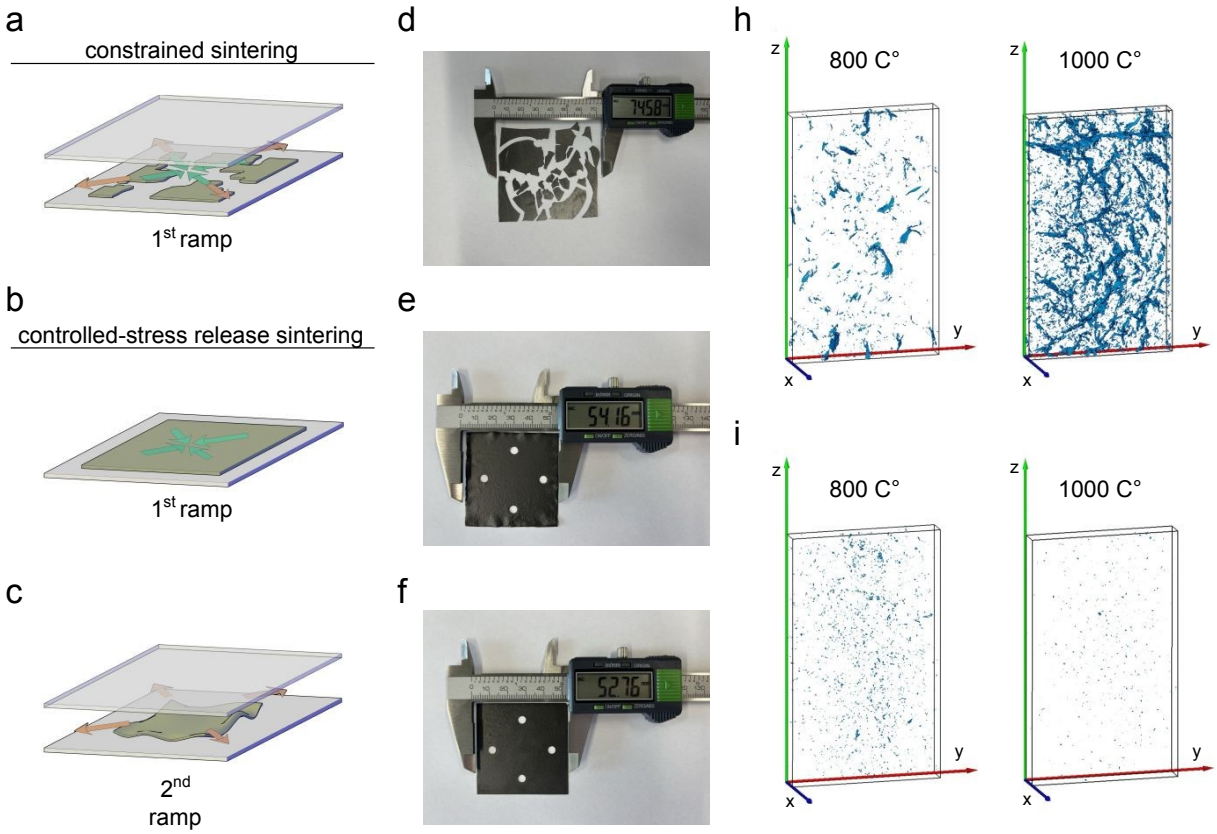

Fig. 2 Effect of constrained and stress-release sintering on LSGM tape morphology. (a) Schematic of constrained sintering. (b) and (c) Schematics of the controlled stress-release sintering during the 1st and 2nd temperature ramps, respectively. Red and blue arrows indicate tensile stresses induced by the setter plate constraint and by shrinkage. (d), (e) and (f) Photographs of the electrolyte after constrained sintering (first ramp), stress-release sintering (first ramp), and stress-release sintering (second ramp). (h) and (i) Computed tomography (CT) analysis of the electrolyte at 800 °C and 1000 °C for constrained and stress-release sintering. Voids are shown in blue, and the remaining regions correspond to solid electrolyte. The scanning volume is 0.14 mm×0.90 mm×1.50 mm.

The sintering of LSGM tapes requires a critical balance between achieving full flatness and managing internal stresses. While high-temperature sintering can produce dense films, the processes of binder burnout (150-400°C) and densification (800-1200°C) generate substantial internal stresses, as confirmed by thermogravimetric analysis and shrinkage measurements (Fig. S1b). Our experiments show that a carefully controlled slow heating profile (Fig. S1c) mitigates these stresses in small-area films. In particular, sintering between rigid alumina setter plates acts as a constrained sintering setup that mechanically restricts out-of-plane deformation and

View Article Online
DOI: 10.1039/D6EY00121A

suppresses warping during binder burnout and densification, thereby helping maintain film flatness in alumina-setter sandwiches.[3,27]

However, this approach failed when scaled to larger-area LSGM tapes. While constrained sintering between setter plates can produce flat electrolyte films (Fig. 2a), as confirmed by 3D profilometry (Fig. S2a), it induces severe cracking in 5 × 5 cm² samples (Fig. 2d). Sintering kinetics studies on constrained ceramic films suggest that the constraint generates in-plane tensile stress, which opposes planar shrinkage, slows densification, and promotes crack formation or the development of porous channels under tensile stress.[28] To overcome this, we developed a controlled stress-release sintering protocol. In the first step, free sintering without a top setter plate allows unconstrained shrinkage, yielding crack-free films (Fig. 2b). Unlike constrained setups, free sintering avoids tensile stress build-up and inhibited densification, allowing defects to heal rather than propagate.[29] Computed tomography (CT) analysis visualized crack evolution during sintering: for constrained samples at 800 °C, isolated voids form (Fig. 2h), which grow, connect, and eventually develop into macro-cracks upon further heating to 1000 °C. In contrast, controlled stress-release sintering shows only a small fraction of voids at 800 °C (Fig. 2i), which decrease during ramping, indicating densification without compromising mechanical integrity. Although cracks are prevented, free-sintered films exhibit significant warping, as shown by 3D profilometry (Fig. 2e and Fig. S2b), making them unsuitable for subsequent electrode deposition and electrochemical testing. To resolve this, a second sintering step applies controlled pressure via setter plates (Fig. 2c), flattening the film while preserving integrity. This two-step process produces flat, fully dense LSGM electrolyte films suitable for cell fabrication (Fig. 2f and Fig. S2c).

The optimized sintering process enables the reliable fabrication of complete cells through subsequent deposition and co-sintering of samaria-doped ceria (SDC) barrier layers, $Co_{0.5}Ni_{0.5}$@SDC cathodes, and LSCF anodes, as confirmed by cross-sectional SEM (Fig. S3). This methodology demonstrates a high reproducibility for 5 × 5 cm² ESCs with active areas of about 17 cm² (Fig. S4), and can be further extended to 10 × 10 cm² with active areas of 69 cm² (Fig. S5), representing an advancement toward manufacturable, industrial-scale SOECs.

Single cell assembly and electrochemical performance

Cell assembly plays a critical role in the electrochemical performance of SOECs, as even minor deviations in the assembly process can lead to significant degradation or failure. In our previous work (Fig. S6),[3] a simplified configuration was employed to test a button cell with an active area of 1 cm², where two Ni back plates were used to host the assembly, mica served as the sealing gasket, Ni foam acted as the cathode current collector, and a gold mesh was applied on the anode side.[3] While such a design ensured uniform pressure distribution and reliable current collection for small cells, it is not feasible for scale-up: the use of gold is cost-inefficient, and the absence of flow channels prevents effective gas distribution in larger-area cells or stacks.

For practical large-area SOECs, the cell is typically sandwiched between two Crofer APU interconnectors (ICs) that provide structural support, current collection, gas flow channels for uniform distribution, and electrode contact, sealed with mica gaskets and uniformly applied pressure.[30-31] In practice, microscopic imperfections on the surfaces, such as bumps on cell and scratches of interconnectors, often result in localized pressure concentrations.[25,32] These pressure non-uniformities can introduce differential mechanical stresses between the cell's anode and cathode sides, increasing the risk of shear-induced cracking during cell mounting. This mechanical vulnerability is closely tied to the flexural strength of the cell, which quantifies its resistance to bending and shear forces. To assess the robustness of our LSGM-based cell, three-point bending tests were conducted, yielding a flexural strength of 468 MPa (Fig. S7a). Maintaining the operational stresses within this mechanical limit is essential for ensuring electrochemical test reliability of the assembled SOEC under practical conditions.

To evaluate and improve the mechanical reliability of the SOEC assembly, we first analyzed the pressure distribution in a conventional IC|Cell|IC configuration (Fig. 3a). The results revealed the presence of localized regions where pressures are simultaneously applied from both the anode and cathode sides (Fig. 3b). These pressure peaks induce substantial shear forces and internal stresses within the cell, with the maximum principal stress reaching 988MPa (Fig. S7b)—far exceeding the cell's measured flexural strength. Under such stress conditions, cell cracking and eventual mechanical failure are unavoidable. Consistent with this result, a gradually decreasing open-circuit potential (OCP) and a reduction in ohmic resistance with increasing current were observed (Fig. 3e and Fig. 3f). This result indicates cell cracking, through which gaseous species mix between the anode and cathode. Oxygen from the anode diffuses to the cathode, lowering the OCP and oxidizing the cathode near the crack. With increasing current, some of the oxidized cathode may be reduced

View Article Online
DOI: 10.1039/D6EY00121A

by electrons or CO, leading to a drop in ohmic resistance as seen in electrochemical impedance spectroscopy.

To address this issue, we propose a modified assembly configuration (Fig. 3c), in which compressive buffer layers are inserted between the ICs and the cell to ensure electrical conductivity under both reductive and oxidative atmospheres. Specifically, Ni foam (NF) is used on the cathode side and LSCF-coated Ni foam (LSCF-NF) on the anode side, forming the configuration which is noted as IC|NF|Cell|LSCF-NF|IC. This configuration leverages the compressibility of Ni foam layers on both sides of the cell, effectively mitigating pressure unevenness and promoting a more uniform pressure distribution (Fig. 3d). In this configuration, the maximum principal stress is reduced to 358 MPa (Fig. S7c), which is below the mechanical limits of the cell. As a result, mechanical integrity is preserved. Electrochemical characterization further confirms this outcome. The OCP remains stable and converges at around 1.03 V (Fig. 3f), and the ohmic resistance remains consistent across different current densities (Fig. 3e).

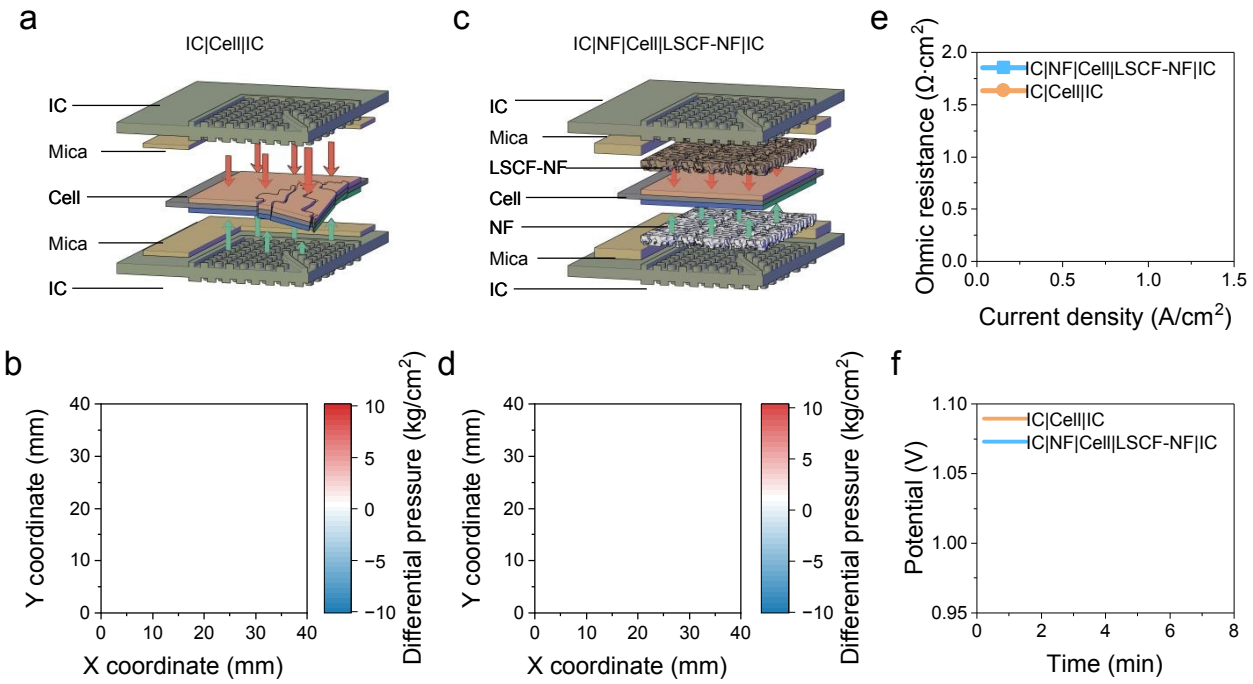

Fig. 3 Cell assembly optimization for mechanical stress mitigation and reliable electrochemical characterization. (a) Schematic of the conventional cell assembly: IC|Cell|IC. (c) Schematic of the optimized configuration with compressive buffer layers: IC|NF|Cell|LSCF-NF|IC. (b) and (d) Differential pressure distributions between the anode and cathode sides for the configurations in (a) and (c), respectively; red and blue indicate pressure from the anode and cathode sides. (e) Ohmic resistance as a function of current density, obtained from electrochemical impedance spectroscopy (EIS) under CO_2, and (f) open-circuit potential (OCP) measured in 20% H_2–N_2, comparing the two configurations.

The electrochemical performance was rigorously evaluated using an IC|NF|Cell|LSCF-NF|IC configuration. For a 5 × 5 cm^2 LSGM ESC with an active area of 17 cm^2, stable operation was achieved at 1 A/cm^2 and 1.21 V under a CO_2 flow rate of 400 sccm (Fig. 4a). At reduced flow rates, higher CO concentrations were achieved in the outlet stream; for example, operating at 0.6 A/cm^2 with 100 sccm CO_2 yielded a 70% CO stream, with the cell voltage increasing modestly from 1.04 V to 1.21 V (Fig. S8a). Under these high-conversion conditions, EIS analysis revealed mass transport limitations, likely arising from CO_2 depletion within the electrode (Fig. S8b). To demonstrate the scalability of the methodology, the performance was validated on a large-format 10 × 10 cm^2 cell (active area of 69 cm^2) using the same assembly. The cell successfully reached a total current of 100 A, though it exhibited a slightly higher potential of 1.26 V at 1

View Article Online
DOI: 10.1039/D6EY00121A

A/cm² (Fig. 4b). This discrepancy is likely attributable to increased mass transfer resistance and less efficient gas distribution inherent to the larger electrode area.

Following the successful demonstration of scale-up, long-term durability was assessed on the 5 × 5 cm² cell. The results showed stable performance over 950 hours at 0.95 A/cm² and 400 sccm CO2. After an initial transient period, the voltage degradation was linear with a remarkably low rate of 0.051 mV/h (Fig. 4b), while the Faradaic efficiency (FE) of CO remained consistently above 90%. This slight decline is primarily attributed to a modest increase in ohmic resistance, as the EIS semicircles—representing polarization resistance—remained nearly unchanged before and after the test (Fig. S9). Post-stability characterization further confirmed the material's robustness. XRD patterns showed that the catalyst retained its NiCo alloy and SDC oxide structure (Fig. S10), and SEM imaging revealed no significant morphological evolution. Cross-sectional TEM/EDS in our previous work established the $Co_{0.5}Ni_{0.5}$@SDC core–shell structure.[3] Here, SEM imaging before and after the durability test (Fig. S11) shows no significant morphological change or particle agglomeration, indicating that the catalyst microstructure remains stable under prolonged operation.

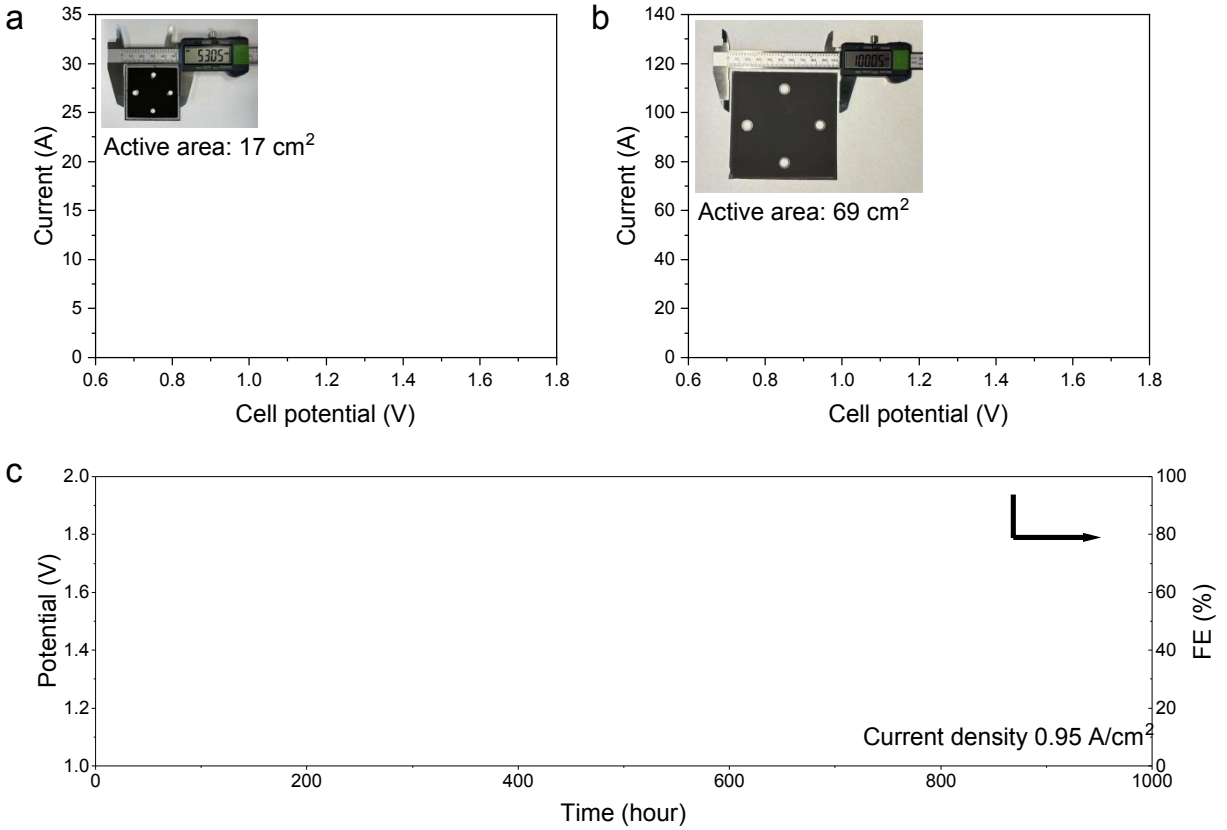

Fig. 4 Electrochemical performance of LSGM ESCs in the optimized assembly configuration. (a) and (b) Polarization (i-V) curves of 5 × 5 cm² and 10 × 10 cm² LSGM ESCs with active areas of 17 cm² and 69 cm², respectively. (c) Long-term galvanostatic electrolysis stability showing the evolution of cell voltage and CO Faradaic efficiency (FE) over time.

Stack assembly and electrochemical performance

To further validate the industrial applicability of LSGM-based ESCs, a short stack comprising five 5 × 5 cm² individual cells was assembled (Fig. 5a). Each unit cell adopted the optimized IC|NF|Cell|LSCF-NF|IC configuration. The cells were electrically connected in series, while cathodic and anodic gas flows were distributed in parallel across all units. In principle, each cell within the stack should experience uniform gas distribution, maintain consistent contact with the interconnectors, and deliver comparable electrochemical performance. Electrochemical characterization confirmed that the five cells exhibited a similar current-voltage (I–V) behavior. At a current density of 1 A/cm², cell 3 showed the lowest operating voltage at 1.20 V, while cell 5 exhibited the highest at 1.24 V (Fig. S12a). EIS further

View Article Online
DOI: 10.1039/D5EY00121A

revealed nearly identical semicircular profiles across all cells (Fig. S12b), indicating uniform electrode performance throughout the stack. Minor variations in high-frequency resistance suggest slight differences in ohmic losses, likely arising from subtle differences in mechanical contact between individual cells and interconnectors. Overall, the stack demonstrated excellent consistency and performance across all five units. It achieved a total current of 30 A at 7.48 V, corresponding to a power output of 225 W and a FE exceeding 90% (Fig. 5b). Subsequently, the stack was operated in galvanostatic mode at a current density of 0.90 A/cm². The voltage profiles of the individual cells remained highly consistent; following an initial transient period, each cell reached a stable operating voltage (Fig. 5c).

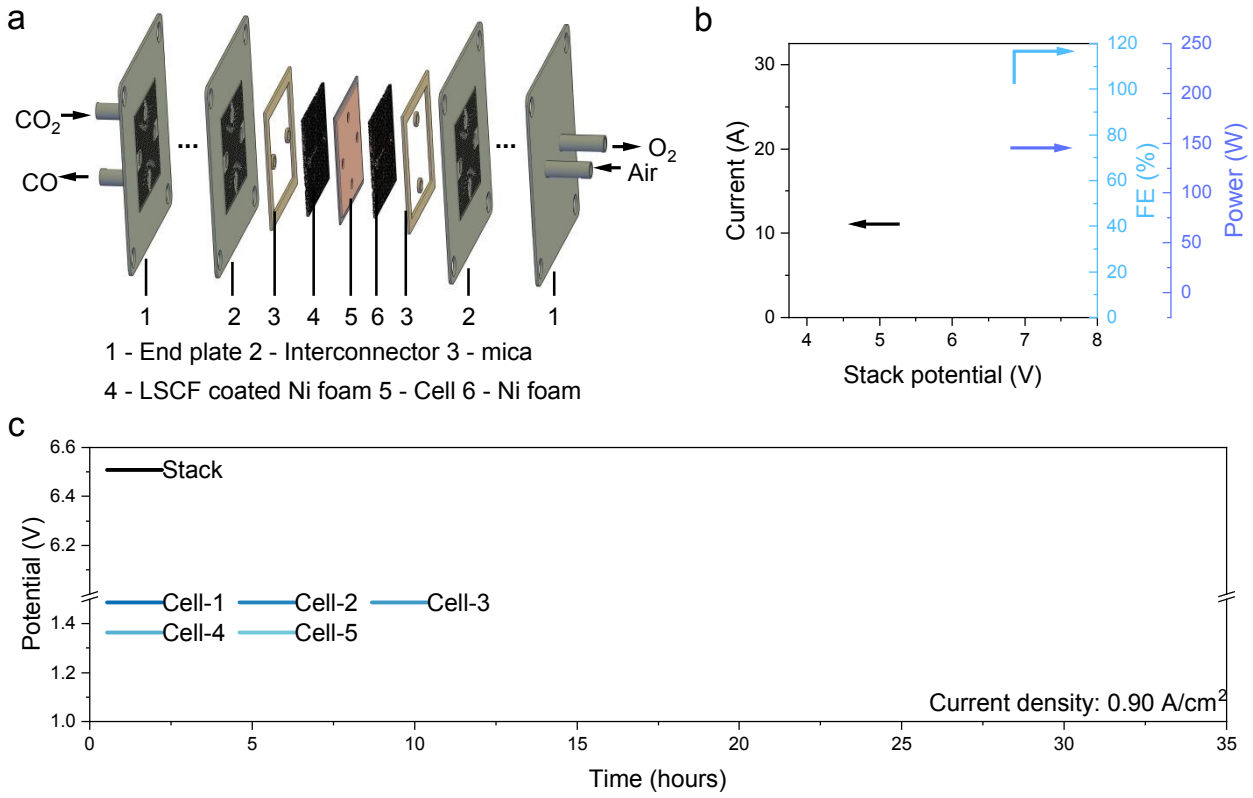

Fig. 5 Performance of a 5-cell stack of LSGM electrolyte-supported SOECs. (a) Schematic of the stack configuration, consisting of (1) end plate, (2) interconnector, (3) mica seal, (4) LSCF-coated Ni foam (anode side), (5) LSGM cell, and (6) Ni foam (cathode side). (b) Stack current–voltage (i–V) curve, Faradaic efficiency (FE), and power output at 800 °C with 2000 sccm CO_2 feed; current is shown on the left axis, FE and power on the right axis. (c) Stack performance in galvanostatic mode with current density of 0.90 A/cm².

Conclusion

This work demonstrates the first successful up-scaling of LSGM-based CO_2 solid oxide electrolysis cells into a multi-cell stack enabled by a systematic engineering strategy for large-area electrolyte-supported SOECs. A two-step sintering protocol was developed to relieve internal stress and eliminate cracking in thin LSGM electrolyte films, ensuring compatibility with electrode deposition and reliable electrochemical testing, while compressive buffer layers based on Ni foam and LSCF-coated Ni foam were introduced between the cells and interconnectors to mitigate localized pressure and prevent mechanical failure during stack assembly. As a result, a 5 × 5 cm² LSGM ESC achieved a current density of 1 A/cm² at 1.21 V with stable operation over 900 h. Building on this cell-level robustness, a five-cell stack with enlarged active area delivered a total electrolysis power of 225 W, corresponding to approximately 1.13 kg day^{-1} of CO production. In contrast to previously reported YSZ-based ESC stacks, which are typically limited to current densities below 0.6 A/cm² and energy efficiencies of ~82%, the present LSGM stack achieves a markedly higher efficiency of 92% at 0.6 A/cm² while operating stably at current densities exceeding 1 A/cm². Compared with prior single-cell LSGM ESC reports, the stack simultaneously offers larger active area and higher total power output, establishing a new

performance benchmark for current density and efficiency in LSGM-based SOEC technology and highlighting its industrial relevance for efficient CO_2-to-CO conversion driven by renewable electricity (Fig. 6).

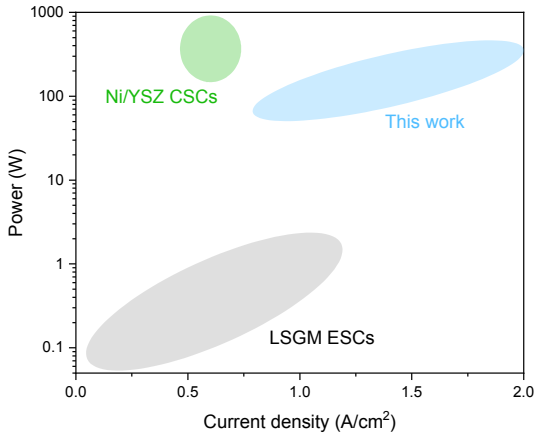

Fig. 6 Comparison of power output versus current density for LSGM-based SOECs reported in the literature. Black points represent performance of LSGM ESCs.[4,13-14,20,33-45] Green points represent performance of Ni/YSZ CSC stack.[46-47] Blue stars represent this work, highlighting the highest-performing and largest-area LSGM stack to date.

Experimental

Chemicals and materials

Nickel(II) nitrate hexahydrate ($Ni(NO_3)_2{\cdot}6H_2O$, 99.9%, ABCR), cobalt(II) nitrate hexahydrate ($Co(NO_3)_2{\cdot}6H_2O$, 98+%, ABCR), citric acid (99.5%, Acros), ethylene glycol (99+%, Brunschwig), cerium(III) nitrate hexahydrate ($Ce(NO_3)_2{\cdot}6H_2O$, 99.5%, ABCR), samarium(III) nitrate hexahydrate ($Sm(NO_3)_3{\cdot}6H_2O$, 99.9%, ABCR), LSGM (Fiaxell SOFC Technologies), copper(II) oxide (CuO, 99%, Sigma), cerium(IV) oxide-samarium doped ($Sm_{0.2}Ce_{0.8}O_{1.9}$, SDC, Sigma), LSCF ($(La_{0.6}0Sr_{0.4})_{0.95}Co_{0.2}Fe_{0.8}O_{3-x}$, Fiaxell SOFC Technologies), dispersant (2%, Fiaxell SOFC Technologies), binder (30%, Fiaxell SOFC Technologies), Ni foam (Fiaxell SOFC Technologies), mica (Fiaxell SOFC Technologies), NiO ink (Fiaxell SOFC Technologies), LSCF ink (Fiaxell SOFC Technologies), and carbon dioxide (CO2, 99.9%, Carbagas) were all used as received without further purification.

Catalyst synthesis

Cathode catalyst, $Co_{0.5}Ni_{0.5}@Ce_{0.8}Sm_{0.2}O_{2-x}$, was synthesized by a sol-gel method. 30 mmol $Co(NO_3)_2{\cdot}6H_2O$, 30 mmol $Ni(NO_3)_2{\cdot}6H_2O$, 12 mmol $Ce(NO_3)_2{\cdot}6H_2O$ and 3 mmol $Sm(NO_3)_3{\cdot}6H_2O$ were dissolved in 40 ml DI water under vigorous stirring. Then, 150 mmol citric acid and 150 mmol ethylene glycol were added to the solution. The solution was heated at 100 °C to form a gel. The mixture was then treated at 300 °C overnight, and then pyrolysis in air at 600 °C for 5 h with ramp up rate of 5 °C/min.

View Article Online
DOI: 10.1039/D6EY00121A

Cell preparation

LSGM electrolyte thin film was fabricated by tape-casting followed by sintering. The slurry for tape-casting was prepared by mixing 20 g LSGM, 16 g dispersant and 20 g binder. The mixture was then ball milled for 1 h, degassed under vacuum, and casted using a tape-casting machine (MTI Corporation) with thickness of 1.5 mm. The yield tape was dried for 48 h at room temperature, tailored into square, and sintered by desired sintering profile. The electrode and buffer layer were deposited on LSGM electrolyte by screen-printing of corresponding ink using a screen-printing machine (Fiaxell SOFC Technologies). The inks were prepared by ball milling of 10 g powder, 10 g dispersant and 4 g binder. First, a SDC buffer layer was screen-printed on both side of LSGM electrolyte to prevent reaction between electrode and electrolyte. Then, $Co_{0.5}Ni_{0.5}@Ce_{0.8}Sm_{0.2}O_{2-x}$ was screen-printed on one side, while LSCF anode (with 35 wt.% SDC to increase O^{2-} conductivity) was screen-printed on another side. A pure LSCF layer was added on top of LSCF anode by screen-printing, to increase electrical conductivity. The printed cell was sintered at 1200 °C for 6 h with a ramp up rate of 2 °C/min to get the LSGM ESCs.

Electrochemical measurement

The single cell and stack test were done in short stack tester kit (Fiaxell SOFC Technologies). In a typical assembly procedure, the mica sealing was first placed on the interconnector, followed by Ni foam. The cathode and anode side of cell was painted with Ni ink and LSCF ink to enhance the electrical conductivity. The cell was then loaded on Ni foam. Another Ni foam was coated with LSCF by dip coating, and put onto the cell. Later, another interconnector was put on top of the LSCF coated Ni foam. For a stack assembly, the previous steps were repeated another 4 times. After, a pressure load of 2 kg/cm^2 was applied on the assembly to ensure good contact and sealing. Electrochemistry was measured by a biologic potentiostat (VMP-300) with a 30-A booster (HCV-3048). The single or stack was assembled in the desired configuration, heated to 800 °C with ramp up rate of 5 °C/min in air. Then, cathode was reduced in 20 vol.% H_2 balanced

with N_2 for 10 min. Next, CO_2 and air were fed to cathode and anode. The flow rate on both electrodes is the same, typically 400 sccm for single cell, and 2000 sccm for stack. The gaseous product form cathode was analyzed by gas chromatograph (SRI Instruments).

The Faradaic efficiency was calculated by equation (1):

$$FE = \frac{n \cdot F \cdot x_{CO,out} \cdot f}{i}$$

where *FE* is the Faradaic efficiency; *n* is the electron transferred per mole of CO produced, which is 2; *F* is the Faradaic constant (96485 C/mol); $x_{CO,out}$ is the molar concentration of CO at the outlet (mol/mol); *f* is the flow rate of the outlet stream (mol/s); *i* is the current in A.

The power of the device was calculated by equation (2):

$$\text{Power} = i \cdot$$

where *i* the current in A and *V* is potential in V.

EIS was measured at the operando conditions, with a perturbation amplitude of 25 mA/cm^2 swing from 100 mHz to 100 kHz.

Characterizations

Thermogravimetric analysis (TGA) of tape-casted LSGM tape was characterized on a TGA 4000 from Perkin Elmer. 10 mg of sample was loaded on a crucible, and heated up in air with ramp up rate of 10 °C/min. To measure the shrinkage of LSGM tape, the length of tape before and after sintering at 100 °C to 1400 °C with 100 °C interval. The shrinkage can be calculated by equation (3):

$$Shrinkage\ at\ X\ °C = \frac{Length\ before\ sintering - Length\ after\ sintering}{Length\ before\ sintering}$$

3D profilometry of LSGM electrolyte thin film was measured by a Bruker Dektak XT surface profiler. The stylus type is 12.5 μm, with a force of 2 mg. The resolution of the mapping is 1 mm in x direction and 1 μm in y direction. A 2 × 2 cm² area on LSGM electrolyte was selected for the mapping.

Flexural strength of LSGM ESC was measured on a Shimadzu EZ-X materials testing machine. A force was applied until fracture of the ESC. the flexural strength can be calculated by equation (4):

$$\sigma_f = \frac{3FL}{2bd^2})$$

where σ_f is the flexural strength, *F* is the maximum force before fracture. *L*, *b* and *d* is the length, width and thickness of the ESC, which are 13 mm, 10 mm and 0.15 mm, respectively.

Pressure difference in assembly was determined by Prescale film from Fujifilm. The pressure distribution on cathode and anode side were measured by placing the film between cell and (LSCF-coated) Ni foam or interconnector. The the apparent pressure load of 2 kg/cm^2 was applied for 5 min for color developing. Next, color distribution on the film was translated into pressure distribution by a protocol from Fujifilm. The pressure difference can then be calculated by equation (5):

$$Pressure\ difference(x,y) = Pressure\ of\ cathode(x,y) - Pressure\ of\ anode\ (x,y) \quad (5)$$

The stress in LSGM ESC can be derived by physical transformations.[48-49] For a planar object, the deflection, *w*(x,y), is governed by biharmonic equation (6):

$$\nabla^2\nabla^2 w(x,y) = \frac{p(x,y)}{D}$$

where *w(x,y)* is the deflection, ∇^2 is the Laplace operator, *p(x,y)* is the 2D pressure difference distribution, and *D* is flexural rigidity of the plate.

The bending and twisting moments can be derived from the second derivatives of *w(x,y)* by equation (7), (8) and (9):

$$M_x(x,y) = -D\left(\frac{\partial^2 w}{\partial x^2} + v\frac{\partial^2 w}{\partial y^2}\right)$$

$$M_y(x,y) = -D\left(\frac{\partial^2 w}{\partial y^2} + v\frac{\partial^2 w}{\partial x^2}\right)$$

$$M_{xy}(x,y) = -D(1-v)\frac{\partial^2 w}{\partial x \partial y}$$

where $M_x(x,y)$ and $M_y(x,y)$ are the bending moments in *x* and *y* direction, $M_{xy}(x,y)$ is the twisting moment, *v* is Poisson's ratio and ∂ is the partial derivative.

The bending stress can be derived from moments by equation (10), (11) and (12):

$$\sigma_x(x,y) = \frac{12M_x z}{h^3})$$

$$\sigma_y(x,y) = \frac{12M_y z}{h^3})$$

$$\tau_{xy}(x,y) = \frac{12M_{xy} z}{h^3})$$

where σ_x and σ_y are normal stress in x and y direction, τ_{xy} is shear stress, h is the plate thickness, and z is half of the plate thickness.

The principal stress, σ_1, can be calculated by equation (13) as a combination of normal stress and shear stress:

$$\sigma_1(x,y) = \frac{\sigma_x + \sigma_y}{2} + \sqrt{\left(\frac{\sigma_x - \sigma_y}{2}\right)^2 + {\tau_{xy}}^2}$$

The above equations are solved numerically by a MALTAB code, and got the distribution of principal stress in plane. To determine if the plate is broken, we can compare the maximum principal stress with flexural strength. If the maximum principal stress is smaller than flexural strength, the cell remains intact, otherwise the cell will break.

Cross-sectional morphology of LSGM ESCs was examined by field-emission scanning electron microscopy (FE-SEM) using a Zeiss Merlin instrument (EPFL Center of MicroNanotechnology, CMi) at an accelerating voltage of 3 kV and a working distance of 5 mm, with a HE-SE2 detector. Phase identification of the catalyst was performed by X-ray diffraction (XRD) using a PANalytical Aeris diffractometer with Cu Kα radiation (λ = 1.5406 Å, 40 kV, 15 mA) and a PIXcel1D-Medipix3 detector, scanning over a 2θ range of 5°–85° in continuous mode.

Author contributions

All authors contributed equally to this work.

Conflicts of interest

There are no conflicts to declare.

Data availability

The data supporting this article have been included as part of the Supplementary Information.

Acknowledgements

This work is supported by EPFL.

References

View Article Online
DOI: 10.1039/D6EY00121A

1 S. Jin, Z. Hao, K. Zhang, Z. Yan and J. Chen, *Angew. Chem.*, 2021, **133**, 20795.
2 S. Overa, B. H. Ko, Y. Zhao and F. Jiao, *Acc. Chem. Res.*, 2022, **55**, 638.
3 W. Ma, J. Morales-Vidal, J. Tian, M.-T. Liu, S. Jin, W. Ren, J. Taubmann, C. Chatzichristodoulou, J. Luterbacher, H. M. Chen and X. Hu, *Nature*, 2025, **641**, 1156.
4 Y. Song, J. Min, Y. Guo, R. Li, G. Zou, M. Li, Y. Zang, W. Feng, X. Yao, T. Liu and X. Bao, *Angew. Chem. Int. Ed.*, 2024, **63**, e202313361.
5 A. Hauch, R. Küngas, P. Blennow, A. B. Hansen, J. B. Hansen, B. V. Mathiesen and M. B. Mogensen, *Science*, 2020, **370**, 6118.
6 H. Liu, M. Yu, X. Tong, Q. Wang and C. Chen, *Chem. Rev.*, 2024, **124**, 10509.
7 S. E. Wolf, F. E. Winterhalder, V. Vibhu, L. B. De Haart, O. Guillon, R. A. Eichel and N. H. Menzler, *J. Mater. Chem. A*, 2023, **11**, 17977.
8 F. Capotondo, M. C. Tucker, B. R. Sudireddy and A. Hagen, *J. Power Sources*, 2025, **646**, 237296.
9 Y. Song, Z. Zhou, Z. Zhang, Y. Zhou, H. Gong, H. Lv, Q. Liu, G. Wang and X. Bao, *J. Mater. Chem. A*, 2018, **6**, 13661.
10 A. Hauch, M. L. Traulsen, R. Kungas and T. L. Skafte, *J. Power Sources*, 2021, **506**, 230108.
11 H. Lv, L. Lin, Z. Zhang, R. Li, Y. Song, H. Matsumoto, N. Ta, C. Zeng, Q. Fu, G. Wang and X. Bao, *Nat. Commun.*, 2021, **12**, 5665.
12 S. Wang, H. Tsuruta, M. Asanuma and T. Ishihara, *Adv. Energy Mater.*, 2015, **5**, 1401003.
13 T. Tan, W. Wang, Z. Qin, M. Zhong, W. Hu, J. Yang, C. Liu and M. Liu, *Adv. Funct. Mater.*, 2022, **32**, 2202878.
14 S. W. Lee, T. H. Nam, S. H. Lee, T. Ishihara, J. T. Irvine and T. H. Shin, *Energy Environ. Sci.*, 2025, **18**, 1205.
15 J. Qian, C. Lin, Z. Chen, J. Huang, N. Ai, S. P. Jiang, X. Zhou, X. Wang, Y. Shao and K. Chen, *Appl. Catal. B: Environ. Energy*, 2024, **346**, 123742.
16 Z. Gao, L. V. Mogni, E. C. Miller, J. G. Railsback and S. A. Barnett, *Energy Environ. Sci.*, 2016, **9**, 1602.
17 S. Sharma, R. Stanley, P. Tiwari, S. Basu, V. Vivekanand and N. Kumari, *Chem. Eng. Technol.*, 2025, **48**, e202400046.
18 D. E. Matkin, I. A. Starostina, M. B. Hanif and D. A. Medvedev, *J. Mater. Chem. A*, 2024, **12**, 25696.
19 W. H. Kan, A. J. Samson and V. Thangadurai, *J. Mater. Chem. A*, 2016, **4**, 17913.
20 S. Liu, Q. Liu and J.-L. Luo, *ACS Catal.*, 2016, **6**, 6219–6228.
21 T. Inagaki, F. Nishiwaki, S. Yamasaki, T. Akbay and K. Hosoi, *J. Power Sources*, 2008, **181**, 274.
22 Y. Du, N. M. Sammes, G. A. Tompsett and M. Bowden, *ECS Proc. Vol.*, 2001, **16**, 311.
23 W. Li, S. Wu, J. Zhu, W. Zhang, W. Guan and J. Li, *J. Eur. Ceram. Soc.*, 2024, **44**, 2242.
24 X. Y. Miao, O. B. Rizvandi, M. Navasa and H. L. Frandsen, *Appl. Energy*, 2021, **293**, 116901.
25 X. Wang, Z. Chen and A. Atkinson, *J. Eur. Ceram. Soc.*, 2013, **33**, 2539.
26 R. Bjørk, H. L. Frandsen and N. Pryds, *J. Am. Ceram. Soc.*, 2015, **98**, 3490.
27 J.-J. Choi, J.-H. Choi, J. Ryu, B.-D. Hahn, J.-W. Kim, C.-W. Ahn, W.-H. Yoon and D.-S. Park, *Thin Solid Films*, 2013, **546**, 418.
28 J. S. Kim, R. A. Rudkin, X. Wang and A. Atkinson, *J. Eur. Ceram. Soc.*, 2011, **31**, 2231.
29 A. Atkinson, J. S. Kim, R. Rudkin, S. Taub and X. Wang, *ECS Trans.*, 2009, **25**, 1531.

View Article Online
DOI: 10.1039/D6EY00121A

30 A. Topcu, B. Ozturk and O. N. Cora, *Int. J. Hydrogen Energy*, 2022, **47**, 3437.
31 M. Rautanen, O. Himanen, V. Saarinen and J. Kiviaho, *Fuel Cells*, 2009, **9**, 753.
32 F. Fleischhauer, A. Tiefenauer, T. Graule, R. Danzer, A. Mai and J. Kuebler, *J. Power Sources*, 2014, **258**, 382.
33 C. Wang, Y. Zhu, Y. Ling, Y. Gong, R. Wang, H. Wang, J. Jin and B. He, *ACS Appl. Mater. Interfaces*, 2023, **15**, 45905.
34 L. Zhang, C. Xu, W. Sun, R. Ren, X. Yang, L. Luo, J. Qiao, Z. Wang, S. Zhen and K. Sun, *Sep. Purif. Technol.*, 2022, **298**, 121475.
35 C. Sun, L. Bian, J. Qi, W. Yu, S. Li, Y. Hou, L. Wang, J. Peng and S. An, *J. Power Sources*, 2022, **521**, 230984.
36 S. Zhang, Y. Jiang, H. Han, Y. Li and C. Xia, *ACS Appl. Mater. Interfaces*, 2022, **14**, 28854.
37 S. K. Kim, Y. I. Kwon, Y. B. Kim, J. Jung, S. Kang and J. H. Joo, *Chem. Eng. J.*, 2022, **444**, 136619.
38 C. Lu, C. Xu, W. Sun, R. Ren, J. Qiao, Z. Wang, K. Sun, G. Pan and Y. Cao, *J. Power Sources*, 2023, **574**, 233134.
39 Q. Liu, Y. Song, R. Li, H. Lv, W. Feng, Y. Shen, X. Zhang, G. Wang and X. Bao, *Int. J. Hydrogen Energy*, 2021, **46**, 19814.
40 E. Wang, L. Zhao, Z. Yang, C. Liu, S. Wang, R. Yang and C. Jin, *J. Colloid Interface Sci.*, 2025, **680**, 605.
41 W. Feng, Y. Song, X. Zhang, H. Lv, Q. Liu, G. Wang and X. Bao, *ChemSusChem*, 2020, **13**, 6290.
42 E. Wang, C. Jin, L. Zhao, Z. Yang, C. Liu, S. Wang, X. Lei, M. Chao, H. Xu and R. Yang, *Chem. Eng. J.*, 2024, **494**, 153129.
43 X. Yang, K. Sun, M. Ma, C. Xu, R. Ren, J. Qiao, Z. Wang, S. Zhen, R. Hou and W. Sun, *Appl. Catal. B: Environ.*, 2020, **272**, 118968.
44 L. Chen, J. Xu, X. Wang and K. Xie, *Int. J. Hydrogen Energy*, 2020, **45**, 11901.
45 H. Li, W. Wang, L. Wang, M. Wang, K. Y. Park, T. Lee, A. Heyden, D. Ding and F. Chen, *ACS Appl. Mater. Interfaces*, 2023, **15**, 43732.
46 M. Riedel, M. P. Heddrich, A. Ansar, Q. Fang, L. Blum and K. A. Friedrich, *J. Power Sources*, 2020, **475**, 228682.
47 F. Thaler, Q. Fang, U. de Haart, L. G. J. De Haart, R. Peters and L. Blum, *ECS Trans.*, 2021, **103**, 363.
48 J. Videla, F. Contreras, H. X. Nguyen and E. Atroshchenko, *Comput. Methods Appl. Mech. Eng.*, 2020, **361**, 112754.
49 Y. Zhou and K. Huang, *Eur. J. Mech. A Solids*, 2024, **108**, 105426.

View Article Online
DOI: 10.1039/D6EY00121A

Data Availability Statement

The data supporting this article have been included as part of the Supplementary Information.